ACS Sustainable Chemistry & Engineering

Research Article

Cite This: ACS Sustainable Chem. Eng. 2019, 7, 7421−7429

pubs.acs.org/journal/ascecg

Solution Processed Nb_2O_5 Electrodes for High Efficient Ultraviolet Light Stable Planar Perovskite Solar Cells

Zenghua Wang,[†,‡] Junjie Lou,[†,‡] Xiaojia Zheng,*[,‡] Wen-Hua Zhang,*[,‡] and Yong Qin*[,†]

[†]Institute of Nanoscience and Nanotechnology, School of Physical Science and Technology, Lanzhou University, 222 South Tianshui Road, Lanzhou, Gansu 730000, China

[‡]Sichuan Research Center of New Materials, Institute of Chemical Materials, China Academy of Engineering Physics, 596 Yinhe Road, Shuangliu, Chengdu 610200, China

Supporting Information

ABSTRACT: TiO_2 is the most widely used electron transport layer (ETL) in high performance perovskite solar cells (PSCs). However, TiO_2 often induces a rapid decay in performance under ultraviolet (UV) light illuminations. So, high performance ETL is urgently needed for PSCs. Here, a new kind of Nb_2O_5 nanoparticles ETL was developed for fabricating efficient planar PSCs with excellent UV stability. The matched band alignment between perovskites and Nb_2O_5 promotes electron injection at the ETL/perovskite interface, and decreases the energy barrier for electron injection. Decreased energy loss during electron transfer from perovskite to Nb_2O_5 and lower recombination rates in the devices contribute to the improved open-circuit voltage (V_{oc}) of PSCs on Nb_2O_5 compared to devices on TiO_2. Power conversion efficiency (PCE) surpassing 20% with a high V_{oc} of 1.19 V was demonstrated for planar PSCs with Nb_2O_5 ETL. The unencapsulated devices based on Nb_2O_5 retained 93% of their initial short-circuit current density (J_{sc}) after 10 h exposure to concentrated 365 nm UV light (46 mW/cm^2), versus 40% for devices based on TiO_2, which was attributed to the excellent chemical stability nature of Nb_2O_5 under UV light.

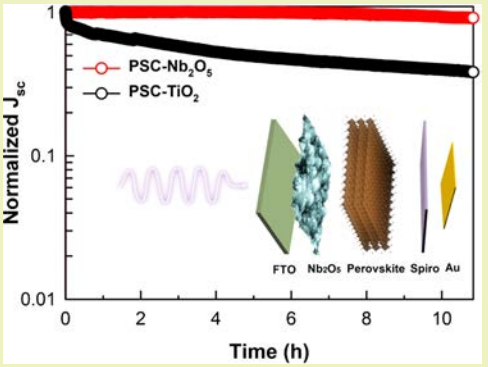

KEYWORDS: *Perovskite solar cell, Electron transport layer, Nb_2O_5, Solution process, Light stability*

INTRODUCTION

Organometal halide perovskites (OHPs) have emerged as a promising candidate for photovoltaic (PV) application owing to their high absorption coefficient, suitable band gap (E_g), long and balanced charge diffusion length, robust fabrication process, etc.[1−5] A certified efficiency as high as 23.7% for a perovskite solar cell (PSC) has been achieved, which shows great promise for next-generation photovoltaic devices.[6] Despite the remarkable progress in PSCs, the instability of perovskite materials and corresponding devices is now one of the biggest challenges for their practical applications.[7−9] It is well-known that PSCs exceeding power conversion efficiency (PCE) of 20% have mainly been demonstrated by employing TiO_2 as the electron transport layer (ETL).[10−12] However, TiO_2 will result in a rapid decay in PCE under UV light illuminations.[13−15] Many efforts have been made to prevent the light-induced degradation, such as surface modification of TiO_2,[16−18] doping of TiO_2 to reduce UV-induced photocatalysis,[19−22] and employing down-conversion phosphor in glass.[23] However, exploring a new type of ETL to replace TiO_2 for fabricating stable PSCs without damaging their performance is critically important and valuable.[24,25]

Many organic semiconductors and metal oxide thin films, such as PCBM,[26] C60,[27] $BaSnO_3$,[28] ZnO,[29] Nb_2O_5,[30] WO_x,[31] and SnO_2,[32] have been prepared and employed as ETLs. PSCs using $BaSnO_3$ and SnO_2 ETLs show excellent stability under light illumination.[28,33] Other than tin based oxides, Nb_2O_5 has attracted considerable attention for its high optical transparency, chemical stability, outstanding conductivity, and well-matched energy levels to the conduction band minimum (CBM) of perovskites. Benefited from its excellent fundamental chemistry and physics, an improved open-circuit voltage (V_{oc}) has been demonstrated in both dye sensitized solar cells (DSSCs) and PSCs.[34−36] PSCs with a PCE as high as 17.2%[30] and 18.59%[37] had been achieved by using sputtered Nb_2O_5 thin film as an effective ETLs, displaying high promise for Nb_2O_5 as ETL for efficient PSCs. Developing a new kind of Nb_2O_5 ETL with much better anti-UV ability and higher PCE of PSCs is critically important and highly valuable.

Here, we report a low-temperature solution route to prepare Nb_2O_5 nanoparticles, and further utilize them as ETL to fabricate PSCs. The PSC fabricated with the Nb_2O_5 compact layer showed a PCE of 20.22% (stabilized PCE of 20.14%) with V_{oc} of 1.19 V. Moreover, these devices exhibited improved UV stability, retaining 93% of the initial short-circuit current density (J_{sc}) under 365 nm UV light exposure (46 mW/cm^2)

Received: February 19, 2019
Revised: March 6, 2019
Published: March 12, 2019

DOI: 10.1021/acssuschemeng.9b00991
ACS Sustainable Chem. Eng. 2019, 7, 7421−7429

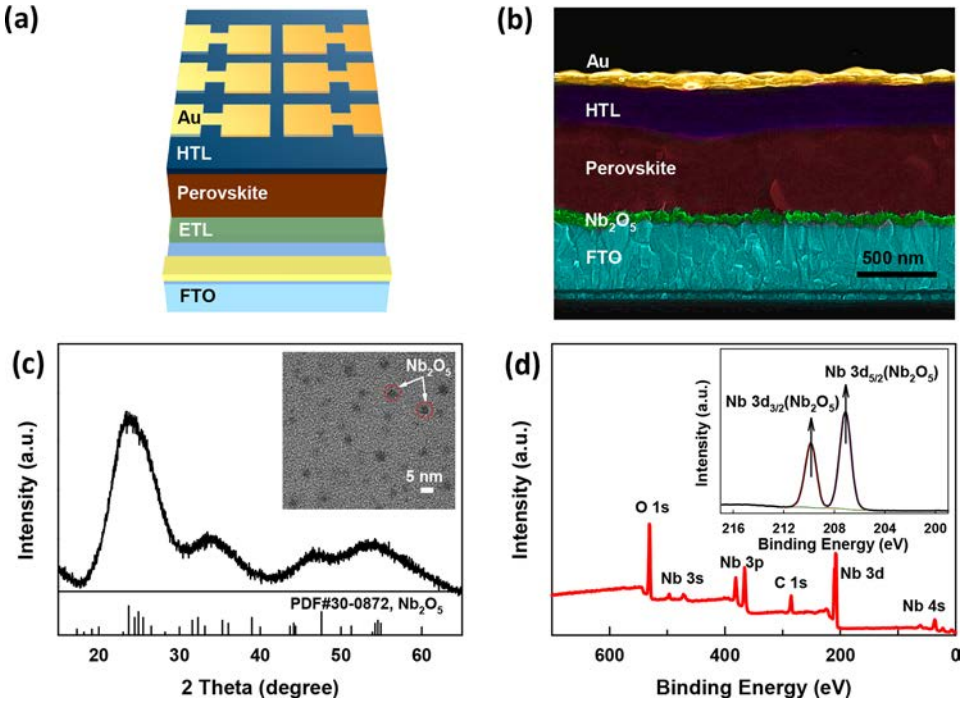

Figure 1. (a) Schematic illustration of the perovskite solar cell. (b) Cross-sectional SEM image of PSCs employing Nb_2O_5 as ETL. (c) X-ray diffraction spectrum and TEM image (inset) and (d) X-ray photoelectron spectra of the as-synthesized Nb_2O_5 nanoparticles.

for 10 h, whereas the device based on TiO_2 retained only 40% of its initial J_{sc}.

EXPERIMENTAL SECTION

Materials. Lead iodide (PbI_2, 99.999%), $TiCl_4$ (99.9%), cesium iodide (CsI, 99.999%), 4-*tert*-butylpyridine (TBP), Li-TFSI, *N*,*N*-dimethylformamide (DMF), and dimethyl sulfoxide (DMSO) were purchased from Aldrich Sigma. Tris(2-(1*H*-pyrazol-1-yl)-4-*tert*-butylpyridine) cobalt(III) bis(trifluoromethylsulfonyl)imide (FK209), formamidine iodide (FAI), methylammonium bromide (MABr), and lead bromide ($PbBr_2$) were purchased from Xi'an p-OLED Corp. HCl (37%) was purchased from Xilong Scientific. $NbCl_5$ (99.9%), benzyl alcohol (anhydrous), ethanol (anhydrous), and methylphenoxide (PhOMe) were purchased from Alfa Aesar. All chemicals used in this work were used as received.

Synthesis of Nb_2O_5 Nanoparticles. $NbCl_5$ (5 mmol) was dispersed by anhydrous ethanol (2 mL, stored in the fridge before use) under stirring to obtain a clear pale yellow solution. After the solution cooled down to room temperature, 10 mL of anhydrous benzyl alcohol was added. The original pale solution became bright yellow after the addition of benzyl alcohol. The mixed solution was loaded into a 20 mL flask, which was firmly sealed and stored without stirring in an oven at 70 °C for 10 h. A white and condensed colloid can be seen at the 6th hour. The product was then washed and precipitated twice as follows: 12 mL of ethanol was added to form a clear dispersion. 60 mL of diethyl ether was then used to precipitate the dispersion. The product Nb_2O_5 nanoparticles were isolated by centrifugation at 5000 rpm for 4 min. The Nb_2O_5 colloidal solution was obtained by dispersing the nanoparticles in anhydrous ethanol (concentration is ~6 mg/mL).

PSC Fabrication. Fluorine-doped tin oxide (FTO) coated glass (NSG 10, Nippon sheet glass, Japan) was used as purchased. The TiO_2 blocking layer was fabricated by a chemical bath deposition method. $TiCl_4$ (0.2 mol) was added in 100 mL of iced deionized water dropwise. After the ice had completely melted, FTO electrodes were immersed in the solution and the hydrothermal growth was conducted in an oven at 80 °C for 70 min. After the reaction had finished, the FTO/TiO_2 substrates were washed with deionized water and dried at 150 °C under ambient condition for 15 min. Nb_2O_5 layers were deposited on bare FTO by spinning the colloidal solution at 2000 rpm for 25 s, and annealed on a hot plate at 150 °C for 15 min in ambient condition. The thickness of the Nb_2O_5 layer was controlled by repeating the deposition process for 1−5 times. The thickness for the film is ~10 nm for once spin-coating process, which almost linearly increases with spin-coating times. Before the deposition of the perovskite layer, the substrates were treated with UV-ozone for 15 min. The anti-solvent assisted crystallization (ASAC) method employing PhOMe as green anti-solvent was used for the deposition of perovskite layers. Perovskite precursor solution was prepared by dissolving FAI (1 M), PbI_2 (1.1 M), MABr (0.2 M), and $PbBr_2$ (0.22 M) in a 4:1 (*V*/*V*) mixture of anhydrous DMF:DMSO. Then, CsI (0.75 M) in DMSO was added to the above solution in 10:95 volume ratios. The mixed solution was aged for 12 h before use. The perovskite deposition process was conducted through a two-step spin-coating program (10 s at 1000 rpm and 40 s at 4000 rpm) with dripping PhOMe during the second step, 10 s before the end. The wet perovskite film was annealed at 110 °C for 20 min. Hole transport material solution containing Spiro-OMeTAD (68 mM), Li-TFSI (32 mM), FK209 (6 mM), and TBP (50 mM) in chlorobenzene and acetonitrile (19/1 in volume ratio) was spun at 4900 rpm for 25 s. Finally, a thin layer (~80 nm) of gold was deposited by thermal evaporation as electrode.

Characterization. X-ray diffraction (XRD) analyzes were performed on an Empyrean X-ray diffractometer with Cu Kα radiation (Panalytical, 2°/min). Scanning electron microscope (SEM) images were obtained under an accelerating voltage of 5 kV (SIGMA HD ZEISS Company). X-ray photoelectron spectroscopy (XPS) analyses were performed on a Thermo escalab 250Xi XPS system, with a 300 μm spot size and energy steps of 0.1 eV. Transmission electron microscopy (TEM) image was obtained at 200 kV (Carl Zeiss SMT Pte, Ltd. Libra 200FE). UV−vis absorption spectra of all samples were recorded on an Evolution 201 spectrophotometer (Thermo Fisher Scientific Corporation). Atomic force microscopy (AFM) topography images were obtained using a Bruker Dimension Icon system in tapping mode under atmospheric condition. Kelvin probe force microscope (KPFM) measurements were performed using amplitude modulation mode with an MESP probe (Co/Cr coated). The work function of the probe was calibrated

DOI: 10.1021/acssuschemeng.9b00991
ACS Sustainable Chem. Eng. 2019, 7, 7421−7429

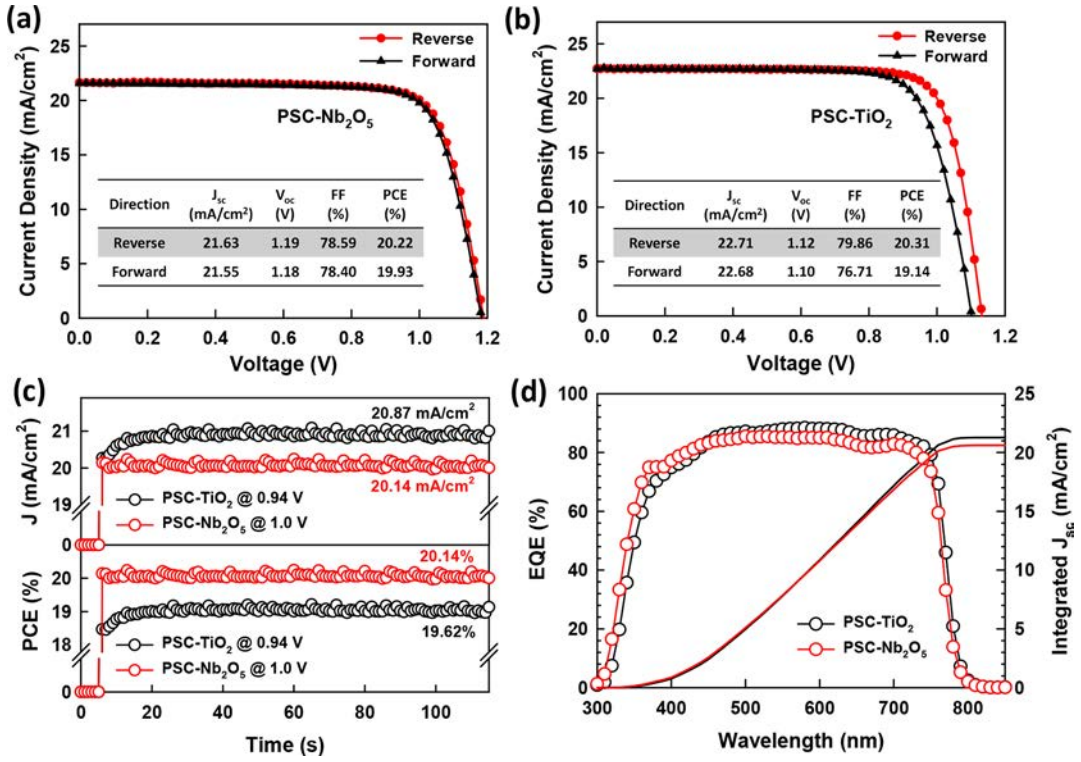

Figure 2. Typical $J-V$ curves of the devices based on (a) Nb_2O_5 and (b) TiO_2 ETLs measured under simulated AM1.5 illumination. (c) The corresponding stabilized current output and PCE around maximum power point as a function of time for the PSCs under 1 sun illumination and (d) EQE spectra of the PSCs.

by freshly cleaned highly ordered pyrolytic graphite (HOPG, with 4.60 eV of constant work function). Current density−voltage measurements were recorded by applying an external potential bias to the cell while recording the generated photocurrent with a digital source meter (Keithley Model 2400) under simulated one sun AM 1.5G illumination at 100 mW/cm^2 (SSF5-3A, Class AAA Solar Simulator, Enlitech) in a glove box. A 50 ms scanning delay was adopted for each data point. Before the test, the exact light intensity was calibrated with a KG5-filited Si reference diode (SRC-2020-KG5-RTD, Enlitech). A metal mask of 0.09 cm^2 was applied for measurement. Electrochemical impedance spectroscopy (EIS) results were recorded by an electrochemical workstation (VMP3 Biologic instruments) at various applied bias under dark condition for frequency from 100 mHz to 100 kHz with an AC amplitude of 30 mV. The steady-state photoluminescence spectrum (PL) was measured with an Edinburgh Instruments Ltd. (FLS980). UV stability measurement was conducted at ambient condition (humidity ∼ 40%, 25 °C) using a 365 nm LED light as UV source. The spectrum of the UV light was measured using an Ocean Optics spectrometer (QE-Pro). The intensity of UV light was calibrated with a photodetector (OPHIR NOVA II). Mott−Schottky (MS) plots for FTO and ETLs analysis were obtained using an electrochemical workstation (VMP3 Biologic instruments) in a standard three-electrode configuration with Ag/AgCl (in saturated KCl) as the reference electrode, and Pt mesh as the counter electrode in 0.1 M NaCl electrolyte. The frequency was 80 mHz, whereas the amplitude potential was 10 mV. External quantum efficiencies (EQE) were measured by a QE-R3011Quantum Efficiency Measurement System (Enlitech) under direct current mode.

RESULTS AND DISCUSSION

Devices were fabricated in a regular planar structure, as shown in Figure 1a. Figure 1b presents the typical cross-sectional SEM image of PSCs employing Nb_2O_5 as ETL. A compact Nb_2O_5 layer, prepared by spinning the colloidal solution on top of FTO glass, was used as the hole blocking layer. A continuous, flat, and dense perovskite film with a thickness of ∼550 nm was deposited by the anti-solvent assisted crystallization (ASAC) method with methoxybenzene (PhOMe) as the green anti-solvent. As shown in Figure 1b and Figure S1, the perovskite films show a smooth surface and 100% coverage, which is consistent with our previous work.[38] On the top of the perovskite layer, an ∼300 nm thick spiro-OMeTAD was deposited as the hole transport material (HTM).

In this work, Nb_2O_5 nanoparticles (NPs) were fabricated through a low-temperature (100 °C) solution process, and then were dispersed into ethanol to form a colloidal solution for film deposition. The Nb_2O_5 NPs solution exhibits a typical Tyndall effect under red laser (Figure S2), confirming its colloidal characteristic.[39] Figure 1c displays the XRD and TEM characterizations of Nb_2O_5 NPs used in this work. The broad peaks shown in the XRD pattern indicate the low crystallinity nature of Nb_2O_5 NPs. The inserted TEM image in Figure 1c shows a 3−5 nm diameter of the used Nb_2O_5 NPs. Figure 1d presents X-ray photoelectron spectroscopy (XPS) spectra of the Nb_2O_5 NPs. A doublet of Nb $3d_{3/2}$ and Nb $3d_{5/2}$ appears, with binding energy (B.E.) values of 209.9 and 207.1 eV, confirming that the Nb element is in the 5^+ oxidation state.[37] There is no residual Cl observed in our low-temperature processed Nb_2O_5, indicating a pure Nb_2O_5 product (Figure 1d). As a reference, PSCs based on TiO_2 ETL were also fabricated, and the device architecture is shown in Figure S3. More detailed information related to the Nb_2O_5 and TiO_2 ETLs can be found in Figures S4 and S5.

It is well-known that the thickness of ETL can affect the device's performance obviously. The high series resistance introduced by too thick ETL will reduce both of the J_{sc} and fill

DOI: 10.1021/acssuschemeng.9b00991
ACS Sustainable Chem. Eng. 2019, 7, 7421−7429

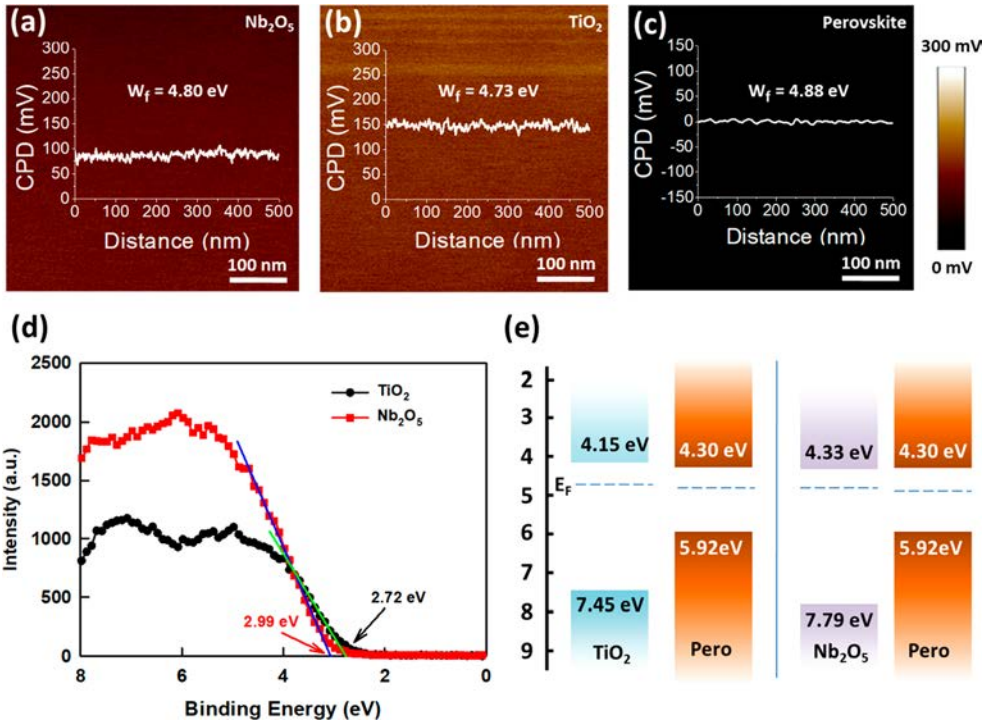

Figure 3. Surface potential images of (a) Nb_2O_5, (b) TiO_2, and (c) perovskite obtained from KPMF measurement. (d) Valence band spectra of Nb_2O_5 (red) and TiO_2 (black) from XPS measurement and (e) band alignment of ETLs and perovskite.

factor (FF) of the cell. However, prominent carrier recombination will happen when the ETL is too thin, due to that the direct contact between perovskite and FTO can result in inferior hole blocking properties. In this work, Nb_2O_5 films with varying thicknesses were prepared by repeating the spin-coating process for 1−5 times (10 nm for one spin-coating process). It is found that the cell performance first increases and then decreases as the thickness of Nb_2O_5 film increases (Figure S6). The photovoltaic parameters of the devices employing the Nb_2O_5 film with different thicknesses are summarized in Table S1. The optimum thickness for the Nb_2O_5 ETL is about 30 nm, which is achieved by repeating the spin-coating process for three times. Figure S7 shows the statistics of the performance for PSCs with optimized experimental condition using Nb_2O_5 and TiO_2 ETLs. The narrow distribution indicates an excellent reproducibility for the devices. Figure 2a presents the typical current density−voltage (J−V) curves of the PSCs measured in reverse scan mode (V_{oc} to J_{sc}) and forward mode (from J_{sc} to V_{oc}) under AM 1.5G illumination (air mass 1.5 global) for PSCs on Nb_2O_5. The device exhibits a V_{oc} of 1.19 V, a J_{sc} of 21.63 mA/cm^2, and an FF of 78.59% under reverse scan, producing a PCE of 20.22%. More importantly, devices based on Nb_2O_5 ETL show negligible J−V hysteresis, showing a PCE of 19.93% under forward scan. In contrast, PSCs based on TiO_2 ETL show obvious J−V hysteresis, with a V_{oc} of 1.12 V, a J_{sc} of 22.71 mA/cm^2, and an FF of 79.86%, yielding an overall PCE of 20.31% under reverse scan, and a V_{oc} of 1.10 V, a J_{sc} of 22.68 mA/cm^2, and an FF of 76.71%, producing an overall PCE of 19.14% under forward scan (Figure 2b). These results clearly show that Nb_2O_5 ETLs can obviously push the V_{oc} of the devices to a much higher value, and 1.19 V is one of the best data for PSCs with similar light absorber in the literature. The steady output current density was monitored with time under an external bias, which is around the maximum power point (Figure 2c). The voltage for maximum power point of PSCs based on Nb_2O_5 ETL is obviously larger than that using TiO_2 ETL, owing to the improved V_{oc}. The current density increased sharply for devices based on Nb_2O_5 when we turned on the light and stabilized at ∼20.14 mA/cm^2, yielding a PCE of ∼20.14%. The current density increased slowly for devices based on TiO_2 ETL when we turned on the light, and gradually stabilized at ∼20.87 mA/cm^2, yielding a PCE of ∼19.62%. Faster dynamic current response always shows lower hysteresis, which agrees well with the J−V results.[40,41] It is worth pointing out that, despite that the PCE for PSCs on Nb_2O_5 is lower than the device on TiO_2 under reverse scan, the stabilized PCE is higher, thanks to the negligible J−V hysteresis effect. The corresponding external quantum efficiency (EQE) spectrum for both cells shown in Figure 2d exhibits a broad plateau above 80% over the spectral range from 400 to 760 nm, indicating an efficient light absorbing, charge transfer, and charge collection in the device. The integrated J_{sc} of 20.61 mA/cm^2 for PSCs on Nb_2O_5 and 21.29 mA/cm^2 for PSCs on TiO_2 are well consistent with the J−V results.

One of the advantages for employing Nb_2O_5 as ETL in PSCs is the high V_{oc}. For a solar cell, the V_{oc} can be written as

$$V_{oc} = \frac{nkT}{q}\ln\left(1 - \frac{G_{sh}V_{oc}}{J_0} + \frac{J_L}{J_0}\right) \quad (1)$$

where J_0, G_{sh}, n, k, and J_L are the diode saturation current density, parallel conductance, diode ideality factor, Boltzmann constant, and photocurrent density, respectively. Considering $J_L \gg G_{sh}V_{oc}$, we know that V_{oc} depends strongly on the J_0, declining dramatically with the increase of J_0. The diode equation provides an expression for the current through a diode as a function of voltage, which can be described by the following equation:

DOI: 10.1021/acssuschemeng.9b00991
ACS Sustainable Chem. Eng. 2019, 7, 7421−7429

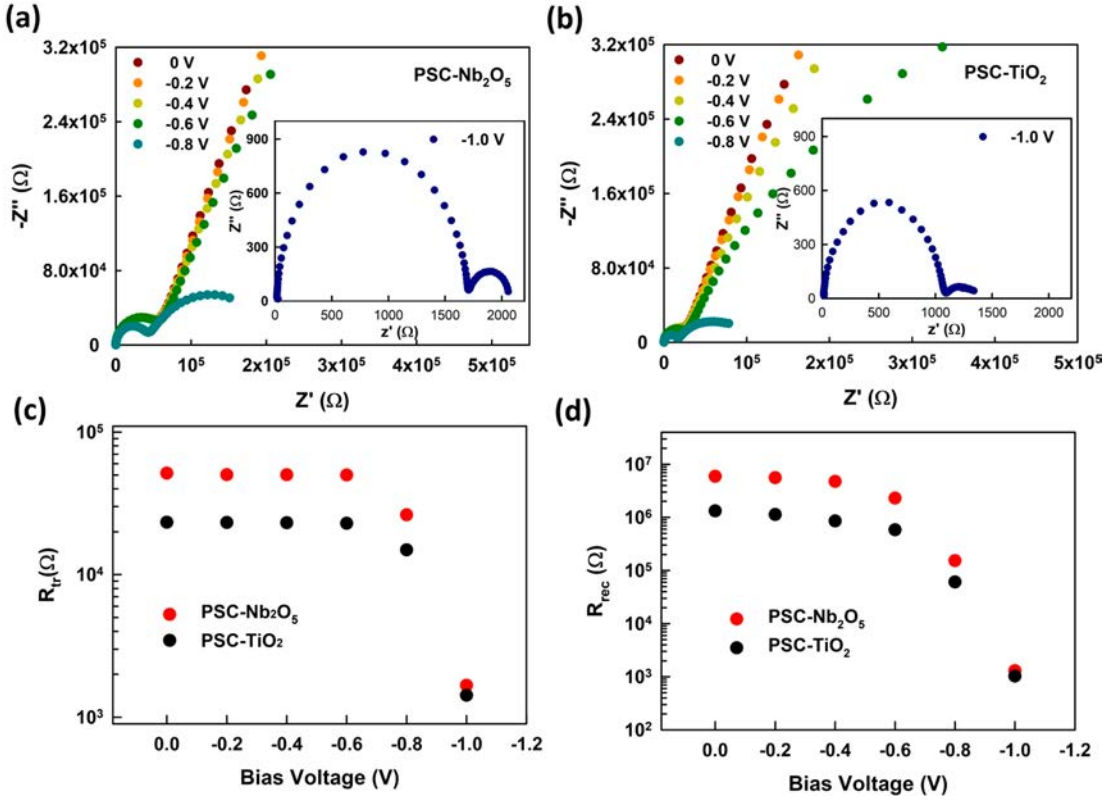

Figure 4. EIS of PSCs based on (a) Nb_2O_5 and (b) TiO_2 ETLs recorded under different applied bias. The inserted figures show the corresponding Nyquist plots measured under the bias of −1.0 V. (c) R_{tr} and (d) R_{rec} derived from the Nyquist plots.

$$J = J_0(e^{qV/nkT} - 1) \quad (2)$$

We measured both the dark $J-V$ curves for the PSCs based on Nb_2O_5 and TiO_2 ETLs. From the semi-logarithmic plots shown in Figure S8, the PSC employing Nb_2O_5 ETL shows lower J_0 value, which accounts for improved V_{oc} in the device.

To further elucidate the mechanism behind the phenomenon of V_{oc} increase, the band alignment scheme for PSCs was studied. The linear part of Tauc plots extracted from UV−vis absorbance measurements was used to calculate the band gap of ETLs and perovskite (Figure S9). We then used Kelvin probe force microscopy (KPFM) to measure contact potential difference (CPD) of the functional layers, from which the work function (W_f) or the position of the Fermi level (E_f) can be inferred. The resulting W_f values are shown in Figure 3a−c. These results are consistent with the flat band potential (U_{fb}), which is derived from the Mott−Schottky (MS) plots (Figure S10). X-ray photoelectron spectroscopy (XPS) has been proved as a suitable method for valence band maximum (VBM) measurements (energy relative to the Fermi level), especially for perovskites.[42] Here, the VBMs for all Nb_2O_5, TiO_2, and perovskite layer were obtained by XPS study, which are shown in Figure 3d and Figure S11. Thus, the energy band diagram for the PSCs can be obtained, which is shown in Figure 3e. The better energy level matching between the perovskites and Nb_2O_5 can decrease the energy barrier for electron extraction, thus decreasing the energy loss during charge transfer at the ETL/perovskite interface, and thereby resulting in a higher V_{oc}.[43]

To gain further insight into how Nb_2O_5 would affect the performance of PSCs, we conducted electrochemical impedance spectroscopy (EIS) to investigate the charge transport and recombination kinetics in PSCs. Nyquist plots shown in Figure 4a,b were measured with AC amplitude of 30 mV at various applied bias under dark condition. There are two typical arcs, where the first arcs at high frequency can be mainly attributed to the charge transport features in bulk materials and the semicircles in the low frequency range mainly represent the charge recombination process at interface.[44,45] The EIS data were fitted with the equivalent circuit diagram given in Figure S12. The equivalent circuit model contains both high frequency elements and low frequency elements. The charge transport resistance (R_{tr}) is ascribed to the small semicircle at high frequency, and the recombination resistance (R_{rec}) assigned to the large arc at low frequency. Due to the same fabrication process except for ETL, so the difference between the R_{tr} and R_{rec} should originate from the ETLs and ETL/perovskite interface. As shown in Figure 4c,d, both R_{tr} and R_{rec} are increased for PSCs based on Nb_2O_5. The higher R_{tr} means a larger transport resistance for electrons in the device, which may be caused by a thicker film for Nb_2O_5 (30 nm) when compared to TiO_2 (10 nm), as well as its inferior crystallinity nature. This higher R_{tr} will deteriorate the J_{sc} value of the devices, which is consistent with the $J-V$ results shown in Figure 2. The increased R_{rec} for PSC based on Nb_2O_5 can be associated primarily with better electron extraction at the ETL/perovskite interface, which results in lower recombination rates, thereby giving higher V_{oc} in PSCs.[46] The steady-state photoluminescence (PL) results shown in Figure S13 also confirm a better electron extraction for Nb_2O_5 film.

Stability under light illumination is one of the challenges for the practical application of PSCs.[47] Therefore, it is better to avoid using TiO_2 ETL for completely overcoming the intrinsic UV light-induced degradation in PCEs. Nb_2O_5 exhibits better

DOI: 10.1021/acssuschemeng.9b00991
ACS Sustainable Chem. Eng. 2019, 7, 7421−7429

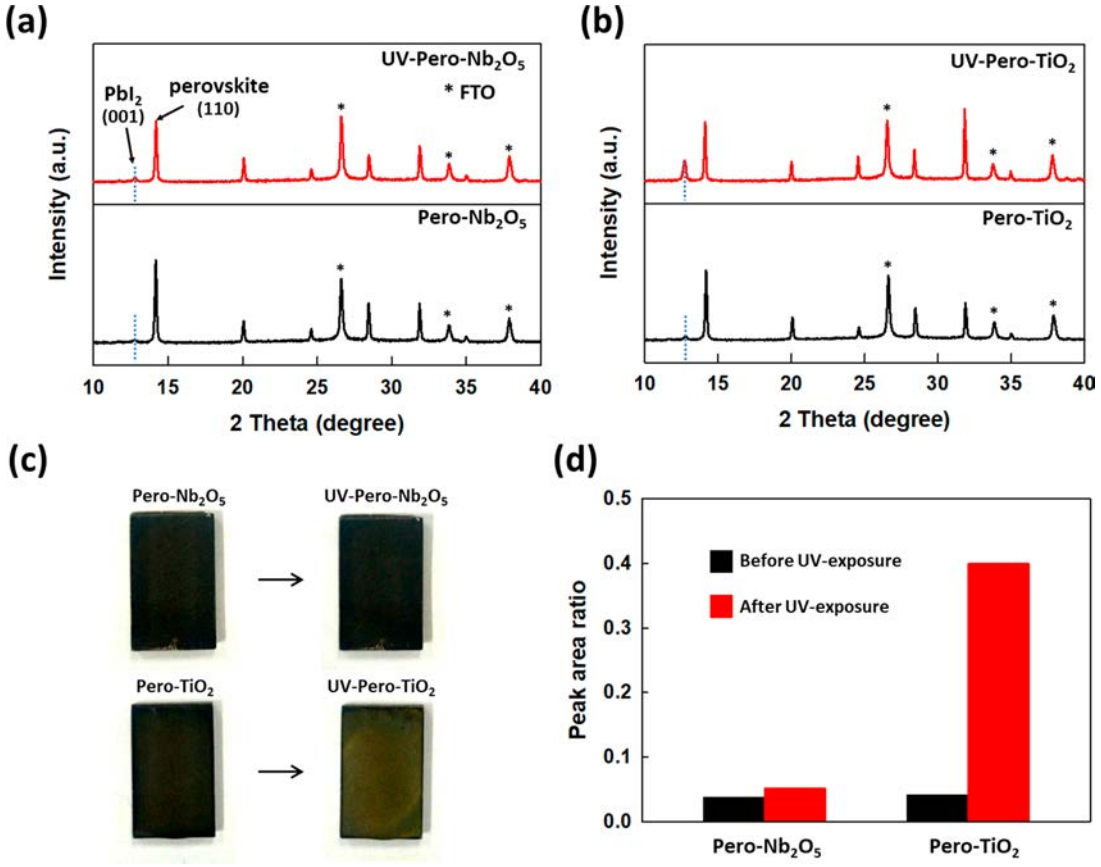

Figure 5. X-ray diffraction spectra of triple cation perovskite films deposited on (a) Nb_2O_5 and (b) TiO_2 before and after UV aging for 10 h. (c) Corresponding optical photograph of the perovskite thin films on different substrates before and after UV irradiation. (d) Peak area ratio of the PbI_2 (001) plane to perovskite (110) plane.

chemical stability relative to that of TiO_2,[48] which may be a benefit for light stability of PSCs. Here, we investigated the stability of perovskite materials deposited on TiO_2 and Nb_2O_5 ETLs under UV light illumination (we denoted the samples as Pero-TiO_2 and Pero-Nb_2O_5, respectively). The UV light was generated by a 365 nm LED light, which showed a half-peak width of 11 nm (Figure S14). The intensity was set to be 46 mW/cm^2, which is about 10 times stronger than the UV section in AM 1.5G.[49] The comparison of diffraction peak areas of PbI_2 (001) at 12.7° and perovskite (110) at 14.16° was used to evaluate the decomposition behavior of perovskite.[50,51] As shown in Figure 5a, after 10 h UV exposure at ambient condition (humidity ∼ 40%), there is no obvious change in their XRD pattern and color (Figure 5c) for Pero-Nb_2O_5. In contrast, we can see an obvious increase of the diffraction peak for PbI_2 when using TiO_2 as the substrate, indicating a low stability of the Pero-TiO_2 (Figure 5b). The color change from dark brown to yellowish after the 10 h UV exposure also indicates an instability nature of Pero-TiO_2 (Figure 5c). Figure 5d further presents the peak area ratio change for (001) of PbI_2 and (110) of perovskite after UV light illumination. The peak area ratio value of Pero-TiO_2 increases by about 10 times, indicating that some perovskite has been decomposed into PbI_2. Meanwhile, the change for Pero-Nb_2O_5 is much smaller. Thus, our results indicate Nb_2O_5 can improve the UV stability of perovskite significantly when compared to TiO_2.

We further examined the UV stability of the planar PSCs on Nb_2O_5 and TiO_2. The UV light soaking experiment was conducted employing PSCs with PCE ∼ 20%. And the J–V curves and parameters presented in Figure S15 and Table S2 were obtained by measuring the devices under one sun illumination in a N_2 atmosphere before and after UV light soaking. The devices made on Nb_2O_5 show substantially improved stability relative to TiO_2 under UV light. A negligible reduction in PCE was witnessed for PSCs using Nb_2O_5 ETL (from 19.97% to 19.51%). On the contrary, the TiO_2 based device suffered an obvious reduction of 20.14% to 12.68% in PCE. The normalized J_{sc} shown in Figure 6a was recorded without encapsulation at ambient condition. Devices based on Nb_2O_5 can retain 93% of their initial J_{sc}, whereas those devices based on TiO_2 can only retain 40% of their initial J_{sc}. Figure 6b,c illustrates the degradation diagram upon UV light exposure for these devices. TiO_2 is known to contain many oxygen vacancies (or Ti^{3+} sites) which interact with molecular oxygen at the surface to form a charge transfer complex (O_2^-–Ti^{4+}).[52−54] The absorbed O_2 on the TiO_2 substrate could generate superoxide anion (O_2^-) under UV light, which might be the primary reason for the decomposition of perovskite in solar cells under light soaking.[55] By replacing TiO_2 with Nb_2O_5, the light-induced O_2^- is suppressed owing to the better chemical stability of Nb_2O_5. Therefore, PSCs with improved UV stability were obtained.

CONCLUSION

In summary, we report a low-temperature solution-processed Nb_2O_5 nanoparticle-formed film as electron transport layer to fabricate PSCs, yielding the highest PCE of 20.22% (stabilized PCE of 20.14%) with a very high V_{oc} of 1.19 V. And PCE of

DOI: 10.1021/acssuschemeng.9b00991
ACS Sustainable Chem. Eng. 2019, 7, 7421−7429

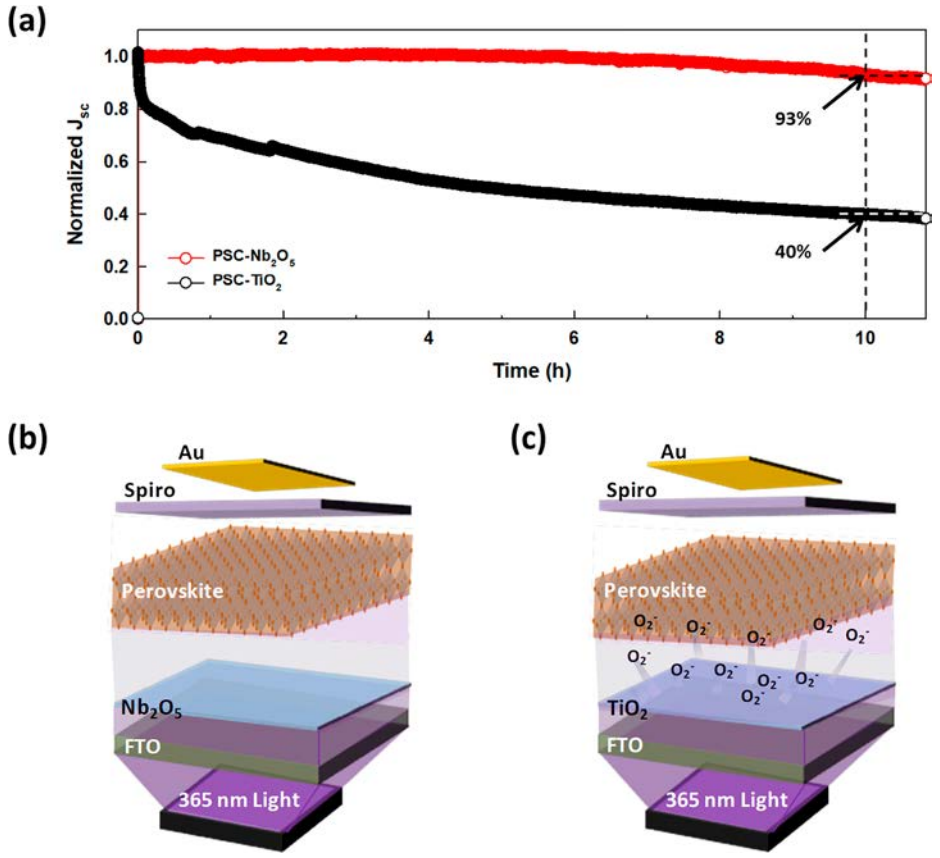

Figure 6. (a) Normalized J_{sc} of unencapsulated PSCs. Degradation diagrams of (b) Nb_2O_5 and (c) TiO_2 based PSCs upon UV exposure.

20.22% and V_{oc} of 1.19 V are the best data for PSCs using Nb_2O_5 as ETL. Moreover, these devices exhibited improved UV stability; a negligible reduction in PCE (from 19.97% to 19.51%) was witnessed for Nb_2O_5 based PSCs before and after UV light soaking, whereas the devices based on TiO_2 showed an obvious reduction from 20.14% to 12.68%. The normalized J_{sc} of Nb_2O_5 PSC retained 93% of the initial J_{sc} under continuous 365 nm UV light exposure (46 mW/cm^2) for 10 h, whereas the TiO_2 based PSCs retained only 40% of their initial J_{sc}.

■ ASSOCIATED CONTENT

Supporting Information

The Supporting Information is available free of charge on the ACS Publications website at DOI: 10.1021/acssuschemeng.9b00991.

Figures S1−S16, showing the morphology of perovskite thin film, ETLs, and PSCs, performance for PSCs using Nb_2O_5 ETL with different thicknesses, $J-V$ curves for PSCs measured under dark condition, Mott−Schottky plots of different ETLs, valence band spectra of perovskite on different ETLs from XPS measurement, equivalent circuit diagram for Nyquist plots fitting, photoluminescence spectrum of perovskite on various substrates, spectrum of the 365 nm UV light, $J-V$ curves for PSCs measured before and after UV light soaking, $J-V$ curves for flexible PSCs, and Tables S1 and S2, showing photovoltaic parameters (PDF)

■ AUTHOR INFORMATION

Corresponding Authors

*E-mail: xiaojia@caep.cn (X.Z.).
*E-mail: whzhang@caep.cn (W.-H.Z.).
*E-mail: qinyong@lzu.edu.cn (Y.Q.).

ORCID

Xiaojia Zheng: 0000-0002-3963-4073
Wen-Hua Zhang: 0000-0002-4381-259X
Yong Qin: 0000-0002-6713-480X

Notes

The authors declare no competing financial interest.

■ ACKNOWLEDGMENTS

The authors acknowledge the financial support from the National Natural Science Foundation of China (Grant No. NSFC21773218), Sichuan Province (Nos. 2017GZ0052, 2018JY0206, 2018RZ0119), China Academy of Engineering Physics (Nos. YZJJLX2018007, 0207, 0202), and Anshan Hifichem Co. Ltd.

■ REFERENCES

(1) Shi, D.; Adinolfi, V.; Comin, R.; Yuan, M.; Alarousu, E.; Buin, A.; Chen, Y.; Hoogland, S.; Rothenberger, A.; Katsiev, K.; Losovyj, Y.; Zhang, X.; Dowben, P. A.; Mohammed, O. F.; Sargent, E. H.; Bakr, O. M. Low trap-state density and long carrier diffusion in organolead trihalide perovskite single crystals. *Science* **2015**, *347*, 519−522.
(2) Li, Z.; Klein, T. R.; Kim, D. H.; Yang, M.; Berry, J. J.; van Hest, M. F. A. M.; Zhu, K. Scalable fabrication of perovskite solar cells. *Nature Rev. Mater.* **2018**, *3*, 18017.

DOI: 10.1021/acssuschemeng.9b00991
ACS Sustainable Chem. Eng. 2019, 7, 7421−7429

(3) Huang, J.; Yuan, Y.; Shao, Y.; Yan, Y. Understanding the physical properties of hybrid perovskites for photovoltaic applications. *Nature Rev. Mater.* **2017**, *2*, 17042.
(4) Chen, H.; Ye, F.; Tang, W.; He, J.; Yin, M.; Wang, Y.; Xie, F.; Bi, E.; Yang, X.; Gratzel, M.; Han, L. A solvent- and vacuum-free route to large-area perovskite films for efficient solar modules. *Nature* **2017**, *550*, 92−95.
(5) Huang, F.; Li, M.; Siffalovic, P.; Cao, G.; Tian, J. From scalable solution fabrication of perovskite films towards commercialization of solar cells. *Energy Environ. Sci.* **2019**, *12*, 518−549.
(6) Leguy, A. M. A.; Frost, J. M.; McMahon, A. P.; Sakai, V. G.; Kockelmann, W.; Law, C. H.; Li, X. E.; Foglia, F.; Walsh, A.; O'Regan, B. C.; Nelson, J.; Cabral, J. T.; Barnes, P. R. F. The dynamics of methylammonium ions in hybrid organic-inorganic perovskite solar cells. *Nat. Commun.* **2015**, *6*, 7124.
(7) Fu, Q.; Tang, X.; Huang, B.; Hu, T.; Tan, L.; Chen, L.; Chen, Y. Recent Progress on the Long-Term Stability of Perovskite Solar Cells. *Adv. Sci.* **2018**, *5*, 1700387.
(8) Park, N.-G.; Gratzel, M.; Miyasaka, T.; Zhu, K.; Emery, K. Towards stable and commercially available perovskite solar cells. *Nat. Energy* **2016**, *1*, 16152.
(9) Li, F.; Yuan, J.; Ling, X.; Zhang, Y.; Yang, Y.; Cheung, S. H.; Ho, C. H. Y.; Gao, X.; Ma, W. A Universal Strategy to Utilize Polymeric Semiconductors for Perovskite Solar Cells with Enhanced Efficiency and Longevity. *Adv. Funct. Mater.* **2018**, *28*, 1706377.
(10) Bi, D.; Yi, C.; Luo, J.; Décoppet, J.-D.; Zhang, F.; Zakeeruddin, S. M.; Li, X.; Hagfeldt, A.; Gratzel, M. Polymer-templated nucleation and crystal growth of perovskite films for solar cells with efficiency greater than 21%. *Nat. Energy* **2016**, *1*, 16142.
(11) Saliba, M.; Matsui, T.; Domanski, K.; Seo, J. Y.; Ummadisingu, A.; Zakeeruddin, S. M.; Correa-Baena, J. P.; Tress, W. R.; Abate, A.; Hagfeldt, A.; Gratzel, M. Incorporation of rubidium cations into perovskite solar cells improves photovoltaic performance. *Science* **2016**, *354*, 206−209.
(12) Yang, W. S.; Noh, J. H.; Jeon, N. J.; Kim, Y. C.; Ryu, S.; Seo, J.; Seok, S. I. High-performance photovoltaic perovskite layers fabricated through intramolecular exchange. *Science* **2015**, *348*, 1234−1237.
(13) Ito, S.; Tanaka, S.; Manabe, K.; Nishino, H. Effects of Surface Blocking Layer of Sb2S3 on Nanocrystalline TiO2 for CH3NH3PbI3 Perovskite Solar Cells. *J. Phys. Chem. C* **2014**, *118*, 16995−17000.
(14) Leijtens, T.; Eperon, G. E.; Pathak, S.; Abate, A.; Lee, M. M.; Snaith, H. J. Overcoming ultraviolet light instability of sensitized TiO2 with meso-superstructured organometal tri-halide perovskite solar cells. *Nat. Commun.* **2013**, *4*, 2885.
(15) Rong, Y.; Hu, Y.; Mei, A.; Tan, H.; Saidaminov, M. I.; Seok, S. I.; McGehee, M. D.; Sargent, E. H.; Han, H. Challenges for commercializing perovskite solar cells. *Science* **2018**, *361*, eaat8235.
(16) Li, W. Z.; Li, J. W.; Niu, G. D.; Wang, L. D. Effect of cesium chloride modification on the film morphology and UV-induced stability of planar perovskite solar cells. *J. Mater. Chem. A* **2016**, *4*, 11688−11695.
(17) Sun, Y.; Fang, X.; Ma, Z. J.; Xu, L. J.; Lu, Y. T.; Yu, Q.; Yuan, N. Y.; Ding, J. N. Enhanced UV-light stability of organometal halide perovskite solar cells with interface modification and a UV absorption layer. *J. Mater. Chem. C* **2017**, *5*, 8682−8687.
(18) Tan, H.; Jain, A.; Voznyy, O.; Lan, X.; García de Arquer, F. P.; Fan, J. Z.; Quintero-Bermudez, R.; Yuan, M.; Zhang, B.; Zhao, Y.; Fan, F.; Li, P.; Quan, L. N.; Zhao, Y.; Lu, Z.-H.; Yang, Z.; Hoogland, S.; Sargent, E. H. Efficient and stable solution-processed planar perovskite solar cells via contact passivation. *Science* **2017**, *355*, 722−726.
(19) Pathak, S. K.; Abate, A.; Ruckdeschel, P.; Roose, B.; Gödel, K. C.; Vaynzof, Y.; Santhala, A.; Watanabe, S.-I.; Hollman, D. J.; Noel, N.; Sepe, A.; Wiesner, U.; Friend, R.; Snaith, H. J.; Steiner, U. Performance and Stability Enhancement of Dye-Sensitized and Perovskite Solar Cells by Al Doping of TiO_2. *Adv. Funct. Mater.* **2014**, *24*, 6046−6055.
(20) Liu, D.; Li, S.; Zhang, P.; Wang, Y.; Zhang, R.; Sarvari, H.; Wang, F.; Wu, J.; Wang, Z.; Chen, Z. D. Efficient planar heterojunction perovskite solar cells with Li-doped compact TiO2 layer. *Nano Energy* **2017**, *31*, 462−468.
(21) Ren, X.; Yang, D.; Yang, Z.; Feng, J.; Zhu, X.; Niu, J.; Liu, Y.; Zhao, W.; Liu, S. F. Solution-Processed Nb:SnO_2 Electron Transport Layer for Efficient Planar Perovskite Solar Cells. *ACS Appl. Mater. Interfaces* **2017**, *9*, 2421−2429.
(22) Yin, G.; Ma, J.; Jiang, H.; Li, J.; Yang, D.; Gao, F.; Zeng, J.; Liu, Z.; Liu, S. F. Enhancing Efficiency and Stability of Perovskite Solar Cells through Nb-Doping of TiO2 at Low Temperature. *ACS Appl. Mater. Interfaces* **2017**, *9*, 10752−10758.
(23) Roh, H. S.; Han, G. S.; Lee, S.; Kim, S.; Choi, S.; Yoon, C.; Lee, J. K. New down-converter for UV-stable perovskite solar cells: Phosphor-in-glass. *J. Power Sources* **2018**, *389*, 135−139.
(24) Shin, S. S.; Suk, J. H.; Kang, B. J.; Yin, W.; Lee, S. J.; Noh, J. H.; Ahn, T. K.; Rotermund, F.; Cho, I. S.; Seok, S. I. Energy-level engineering of the electron transporting layer for improving open-circuit voltage in dye and perovskite-based solar cells. *Energy Environ. Sci.* **2019**, *12*, 958.
(25) Ke, W.; Fang, G.; Liu, Q.; Xiong, L.; Qin, P.; Tao, H.; Wang, J.; Lei, H.; Li, B.; Wan, J.; Yang, G.; Yan, Y. Low-Temperature Solution-Processed Tin Oxide as an Alternative Electron Transporting Layer for Efficient Perovskite Solar Cells. *J. Am. Chem. Soc.* **2015**, *137*, 6730−6733.
(26) Zhang, Y.; Hu, X.; Chen, L.; Huang, Z.; Fu, Q.; Liu, Y.; Zhang, L.; Chen, Y. Flexible, hole transporting layer-free and stable $CH_3NH_3PbI_3$/PC61BM planar heterojunction perovskite solar cells. *Org. Electron.* **2016**, *30*, 281−288.
(27) Yoon, H.; Kang, S. M.; Lee, J. K.; Choi, M. Hysteresis-free low-temperature-processed planar perovskite solar cells with 19.1% efficiency. *Energy Environ. Sci.* **2016**, *9*, 2262−2266.
(28) Shin, S. S.; Yeom, E. J.; Yang, W. S.; Hur, S.; Kim, M. G.; Im, J.; Seo, J.; Noh, J. H.; Seok, S. I. Colloidally prepared La-doped $BaSnO_3$ electrodes for efficient, photostable perovskite solar cells. *Science* **2017**, *356*, 167−171.
(29) Zhang, P.; Wu, J.; Zhang, T.; Wang, Y. F.; Liu, D. T.; Chen, H.; Ji, L.; Liu, C. H.; Ahmad, W.; Chen, Z. D.; Li, S. B. Perovskite Solar Cells with ZnO Electron-Transporting Materials. *Adv. Mater.* **2018**, *30*, 1703737.
(30) Ling, X.; Yuan, J.; Liu, D.; Wang, Y.; Zhang, Y.; Chen, S.; Wu, H.; Jin, F.; Wu, F.; Shi, G.; Tang, X.; Zheng, J.; Liu, S. F.; Liu, Z.; Ma, W. Room-Temperature Processed Nb2O5 as the Electron-Transporting Layer for Efficient Planar Perovskite Solar Cells. *ACS Appl. Mater. Interfaces* **2017**, *9*, 23181−23188.
(31) Wang, K.; Shi, Y.; Gao, L.; Chi, R.; Shi, K.; Guo, B.; Zhao, L.; Ma, T. W(Nb)Ox-based efficient flexible perovskite solar cells: From material optimization to working principle. *Nano Energy* **2017**, *31*, 424−431.
(32) Anaraki, E. H.; Kermanpur, A.; Steier, L.; Domanski, K.; Matsui, T.; Tress, W.; Saliba, M.; Abate, A.; Gratzel, M.; Hagfeldt, A.; Correa-Baena, J. P. Highly efficient and stable planar perovskite solar cells by solution-processed tin oxide. *Energy Environ. Sci.* **2016**, *9*, 3128−3134.
(33) Wan, F.; Qiu, X.; Chen, H.; Liu, Y.; Xie, H.; Shi, J.; Huang, H.; Yuan, Y.; Gao, Y.; Zhou, C. Accelerated electron extraction and improved UV stability of TiO_2 based perovskite solar cells by SnO_2 based surface passivation. *Org. Electron.* **2018**, *59*, 184−189.
(34) Kogo, A.; Numata, Y.; Ikegami, M.; Miyasaka, T. Nb_2O_5 Blocking Layer for High Open-circuit Voltage Perovskite Solar Cells. *Chem. Lett.* **2015**, *44*, 829−830.
(35) Jose, R.; Thavasi, V.; Ramakrishna, S. Metal Oxides for Dye-Sensitized Solar Cells. *J. Am. Ceram. Soc.* **2009**, *92*, 289−301.
(36) Fernandes, S. L.; Veron, A. C.; Neto, N. F. A.; Nuesch, F. A.; Dias da Silva, J. H.; Zaghete, M. A.; de O. Graeff, C. F. Nb_2O_5 hole blocking layer for hysteresis-free perovskite solar cells. *Mater. Lett.* **2016**, *181*, 103−107.
(37) Feng, J. S.; Yang, Z.; Yang, D.; Ren, X. D.; Zhu, X. J.; Jin, Z. W.; Zi, W.; Wei, Q. B.; Liu, S. Z. E-beam evaporated Nb_2O_5 as an effective electron transport layer for large flexible perovskite solar cells. *Nano Energy* **2017**, *36*, 1−8.

DOI: 10.1021/acssuschemeng.9b00991
ACS Sustainable Chem. Eng. 2019, 7, 7421−7429

(38) Zhang, M.; Wang, Z.; Zhou, B.; Jia, X.; Ma, Q.; Yuan, N.; Zheng, X.; Ding, J.; Zhang, W.-H. Green Anti-Solvent Processed Planar Perovskite Solar Cells with Efficiency Beyond 19%. *Solar RRL* **2018**, *2*, 1700213.
(39) Yang, S.; Niu, W.; Wang, A. L.; Fan, Z.; Chen, B.; Tan, C.; Lu, Q.; Zhang, H. Ultrathin Two-Dimensional Organic-Inorganic Hybrid Perovskite Nanosheets with Bright, Tunable Photoluminescence and High Stability. *Angew. Chem., Int. Ed.* **2017**, *56*, 4252−4255.
(40) Zheng, X.; Wu, C.; Jha, S. K.; Li, Z.; Zhu, K.; Priya, S. Improved Phase Stability of Formamidinium Lead Triiodide Perovskite by Strain Relaxation. *ACS Energy Lett.* **2016**, *1*, 1014−1020.
(41) Zheng, X.; Chen, B.; Wu, C.; Priya, S. Room temperature fabrication of $CH_3NH_3PbBr_3$ by anti-solvent assisted crystallization approach for perovskite solar cells with fast response and small J−V hysteresis. *Nano Energy* **2015**, *17*, 269−278.
(42) Miller, E. M.; Zhao, Y.; Mercado, C. C.; Saha, S. K.; Luther, J. M.; Zhu, K.; Stevanovic, V.; Perkins, C. L.; van de Lagemaat, J. Substrate-controlled band positions in $CH_3NH_3PbI_3$ perovskite films. *Phys. Chem. Chem. Phys.* **2014**, *16*, 22122−22130.
(43) Cai, B.; Xing, Y. D.; Yang, Z.; Zhang, W. H.; Qiu, J. S. High performance hybrid solar cells sensitized by organolead halide perovskites. *Energy Environ. Sci.* **2013**, *6*, 1480−1485.
(44) Bag, M.; Renna, L. A.; Adhikari, R. Y.; Karak, S.; Liu, F.; Lahti, P. M.; Russell, T. P.; Tuominen, M. T.; Venkataraman, D. Kinetics of Ion Transport in Perovskite Active Layers and Its Implications for Active Layer Stability. *J. Am. Chem. Soc.* **2015**, *137*, 13130−13137.
(45) Jamnik, J.; Maier, J. Treatment of the Impedance of Mixed Conductors Equivalent Circuit Model and Explicit Approximate Solutions. *J. Electrochem. Soc.* **1999**, *146*, 4183−4188.
(46) Chen, Y.; Yang, Z.; Wang, S.; Zheng, X.; Wu, Y.; Yuan, N.; Zhang, W. H.; Liu, S. F. Design of an Inorganic Mesoporous Hole-Transporting Layer for Highly Efficient and Stable Inverted Perovskite Solar Cells. *Adv. Mater.* **2018**, *30*, 1805660.
(47) Gholipour, S.; Saliba, M. From Exceptional Properties to Stability Challenges of Perovskite Solar Cells. *Small* **2018**, *14*, 1802385.
(48) Rani, R. A.; Zoolfakar, A. S.; O'Mullane, A. P.; Austin, M. W.; Kalantar-Zadeh, K. Thin films and nanostructures of niobium pentoxide: fundamental properties, synthesis methods and applications. *J. Mater. Chem. A* **2014**, *2*, 15683−15703.
(49) Li, W. Z.; Zhang, W.; Van Reenen, S.; Sutton, R. J.; Fan, J. D.; Haghighirad, A. A.; Johnston, M. B.; Wang, L. D.; Snaith, H. J. Enhanced UV-light stability of planar heterojunction perovskite solar cells with caesium bromide interface modification. *Energy Environ. Sci.* **2016**, *9*, 490−498.
(50) Yang, B.; Dyck, O.; Poplawsky, J.; Keum, J.; Das, S.; Puretzky, A.; Aytug, T.; Joshi, P. C.; Rouleau, C. M.; Duscher, G.; Geohegan, D. B.; Xiao, K. Controllable Growth of Perovskite Films by Room-Temperature Air Exposure for Efficient Planar Heterojunction Photovoltaic Cells. *Angew. Chem., Int. Ed.* **2015**, *54*, 14862−14865.
(51) Wang, C.; Zhang, C.; Wang, S.; Liu, G.; Xia, H.; Tong, S.; He, J.; Niu, D.; Zhou, C.; Ding, K.; Gao, Y.; Yang, J. Low-Temperature Processed, Efficient, and Highly Reproducible Cesium-Doped Triple Cation Perovskite Planar Heterojunction Solar Cells. *Solar RRL* **2018**, *2*, 1700209.
(52) Henderson, M. A.; Epling, W. S.; Perkins, C. L.; Peden, C. H. F.; Diebold, U. Interaction of Molecular Oxygen with the Vacuum-Annealed TiO_2 (110) Surface: Molecular and Dissociative Channels. *J. Phys. Chem. B* **1999**, *103*, 5328−5337.
(53) Schwanitz, K.; Weiler, U.; Hunger, R.; Mayer, T.; Jaegermann, W. Synchrotron-Induced Photoelectron Spectroscopy of the Dye-Sensitized Nanocrystalline TiO_2/Electrolyte Interface: Band Gap States and Their Interaction with Dye and Solvent Molecules. *J. Phys. Chem. C* **2007**, *111*, 849−854.
(54) Cronemeyer, D. C. Infrared Absorption of Reduced Rutile TiO2 Single Crystals. *Phys. Rev.* **1959**, *113*, 1222−1226.
(55) Pathak, S. K.; Abate, A.; Leijtens, T.; Hollman, D. J.; Teuscher, J.; Pazos, L.; Docampo, P.; Steiner, U.; Snaith, H. J. Towards Long-Term Photostability of Solid-State Dye Sensitized Solar Cells. *Adv. Energy Mater.* **2014**, *4*, 1301667.

DOI: 10.1021/acssuschemeng.9b00991
ACS Sustainable Chem. Eng. 2019, 7, 7421−7429